

SUPPORTING INFORMATION

Reductive Sequestration of Pertechnetate (TcO_4^-) by Nano Zero-valent Iron Transformed by Abiotic Sulfide

*Dimin Fan, Roberto P. Anitori, Bradley M. Tebo, Paul G. Tratnyek**

Division of Environmental and Biomolecular Systems
Oregon Health & Science University
20000 NW Walker Road, Portland, OR 97006

Juan S. Lezama Pacheco

Stanford Synchrotron Radiation Lightsource
Menlo Park, CA 94025

Current Address

School of Earth Sciences, Environmental Earth System Science Department,
Stanford University
Stanford, CA 94305-4216

Ravi K. Kukkadapu, Mark H. Engelhard, Mark E. Bowden,

Libor Kovarik, Bruce W. Arey

Environmental Molecular Sciences Laboratory, Pacific Northwest National
Laboratory
Richland, WA 99354

*Corresponding author:

Email: tratnyek@ebs.ogi.edu, Phone: 503-748-1023, Fax: 503-748-1464

Contents

Section 1. Characterization and Properties of Original and Sulfidated nZVI (Table S1, S2, S3, Figure S1, S2, S3)	S2
Section 2. Batch Tc Reduction Kinetics under High nZVI Dose (Figure S4, S5)	S10
Section 3. Evidence of Colloidal Tc Formation (Figure S6)	S12
Section 4. SEMs and TEMs of Sulfidated nZVI Exposed to TcO_4^- (Figure S7, S8)	S12
Section 5. Additional XAS Information (Table S4, Figure S9, S10, S11)	S14
Section 6. Geochemical Speciation Modeling of Tc/Fe/S (Figure S12)	S17
References in Supporting Information	S19

1. Characterization and Properties of Pristine nZVI and Sulfidated nZVI

Composition of Hanford artificial groundwater (HS300)

Table S1. Recipe for Hanford artificial groundwater (HS300a)

Component	Concentration (mM)
NaHCO ₃	1.44
KHCO ₃	0.16
MgCl ₂ •6H ₂ O	0.51
CaCl ₂ •2H ₂ O	0.37
CaSO ₄ •2H ₂ O	0.63
NaH ₂ PO ₄	1.50
NH ₄ Cl	4.70
HEPES	30.00 ^b

^a Modified from SGW1 medium in Lee et al.¹

^b 30 mM HEPES provides additional buffer capacity to neutralize pH increase from sodium sulfide.

Methods

Micro X-ray Diffraction.

Powders for diffraction analysis were loaded into 0.5 mm glass capillaries (Charles Supper Co., MA) under nitrogen atmosphere and sealed with wax. Diffraction data were recorded by the 2D image plate of a Rigaku D/Max Rapid II diffractometer. Cr K α radiation ($\lambda = 2.2910 \text{ \AA}$) focused through a 300 μm diameter collimator was used, which avoids the high background produced from fluorescence of Fe-containing samples. The 2-dimensional diffraction data were integrated between 10 and 160° 2 θ to give powder traces. Backgrounds were removed using the JADE software (Materials Data Inc. CA) by subtracting a trace from an empty capillary and additionally fitting a smooth spline curve.

Mössbauer Spectroscopy.

Sample preparation for Mössbauer spectroscopy is identical to the procedures reported in Peretyazhko et al.² Mössbauer spectra of the samples were collected using either a WissEl Elektronik (Germany) or Web Research Company (St. Paul, MN) instruments that included a closed-cycle cryostat SHI-850 obtained from Janis Research (Wilmington, MA), a Sumitomo CKW-21 He compressor unit (Wilmington, MA), and an Ar-Kr proportional counter detector

with WissEl setup or a Ritverc (St. Petersburg, Russia) NaI detection system. A $^{57}\text{Co}/\text{Rh}$ source (50 mCi to 75 mCi, initial strength) was used as the gamma energy source. With the WissEl setups, the transmitted counts were stored in a multichannel scalar (MCS) as a function of energy (transducer velocity) using a 1024-channel analyzer. The setups data were folded to 512 channels to provide a flat background and a zero-velocity position corresponding to the center shift (CS) of a metal Fe foil at room temperature (RT). Calibration spectra were obtained with a 25 μm thick Fe foil (Amersham, England) placed in the same position as the samples to minimize any geometry errors. The Mössbauer data were modeled with RecoilTM software (University of Ottawa, Canada) using a Voigt-based structural fitting routine.

X-Ray Photoelectron Spectroscopy.

The XPS analyses were conducted using a Physical Electronics Quanterra Scanning ESCA Microprobe with a focused monochromatic Al Ka X-ray source (1486.7 eV) source and a spherical section analyzer. The mineral powder sample was mounted inside a nitrogen recirculated glove box operated at <0.5 ppm O₂. The samples were pressed onto double sided Scotch tape (#34-8507-5367-3) and supported by 1 cm x 3 cm clean flat Si (100) wafers. The individual Si wafer pieces were then mounted onto the standard Physical Electronics 75 mm x 75 mm sample holder using 2-56 stainless steel screws. The sample holder was then placed into the XPS vacuum introduction system and pumped to <1 x 10⁻⁶ Torr using a turbomolecular pumping system prior to introduction into the main ultra high vacuum system. The main vacuum system pressure is maintained at <5 x 10⁻⁹ Torr during analysis and pumped using a series of sputter ion pumps and turbo-molecular pumps. For large collections of mineral particles, the X-ray beam was operated at approximately 100 W, focused to 100 μm diameter, and rastered over a 1.3 mm x 0.1 mm rectangle on the sample. The X-ray beam is incident normal to the sample and the photoelectron detector is at 45° off-normal. High energy resolution spectra were collected using a pass-energy of 69.0 eV with a step size of 0.125 eV. For the Ag 3d_{5/2} line, these conditions produced a FWHM of 0.91 eV. The sample experienced variable degrees of charging. Low energy electrons at ~1 eV, 20 μA and low energy Ar⁺ ions were used to minimize this charging. The spectra were aligned to a carbon peak energy of 285.0 eV (adventitious carbon). The compositional results were obtained using the standard sensitivity factors in the Phi Multipak software package using peak area intensities after a Shirley background subtraction.

Transmission Electron Microscopy (TEM).

The samples without exposure to Tc were prepared for TEM observations by dispersing a dry powder on a lacey-carbon coated 200 mesh Cu TEM grids under anaerobic conditions. In a subsequent step of loading the sample into the TEM, however, the samples were exposed to aerobic conditions for a period of few minutes. TEM conventional and high-resolution images were performed with spherical aberration corrected FEI Titan 80-300 operated at 300kV. The elemental analysis was performed with EDAX Si (Li) EDS detector and a subsequent analysis was performed with TIA software.

BET Surface Area Measurements

100 to 200 mg of material was placed in a sealed BET vial and weighed (pre-drying weight). The sample in the BET vial was then placed in the VacPrep 061 in which the samples were heated under flowing UHP N₂ at 200°C. At selected times, the samples were allowed to cool and then weighed (after-drying weight). After samples were dried, surface area was measured by N₂ adsorption using a Micrometrics Gemini V surface area and pore size analyzer.

Results

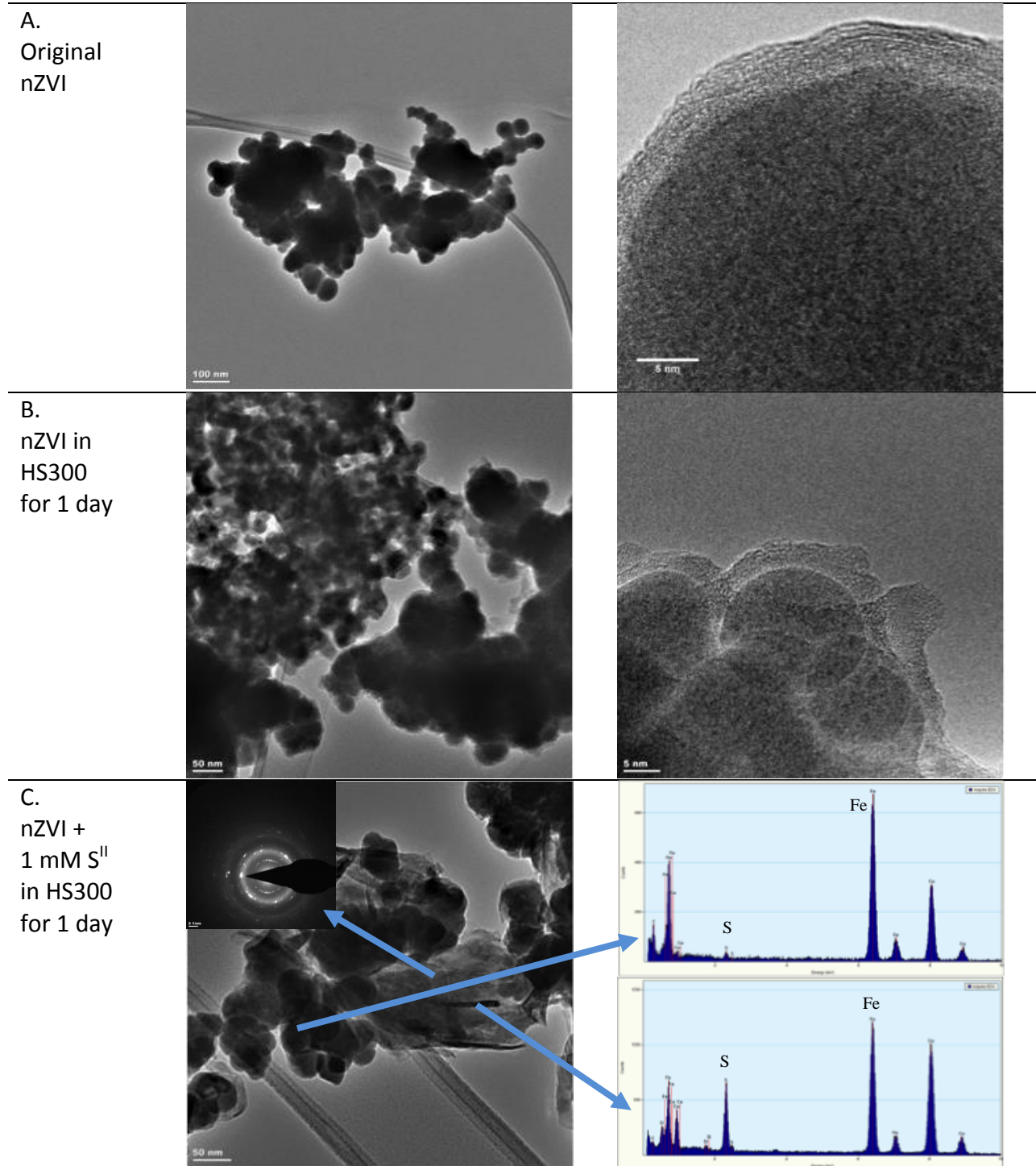


Figure S1. Transmission electron micrographs of **(A)** freshly prepared nZVI: long chain structure connecting primary particles (left), primary particle with core-shell structure (right); **(B)** nZVI exposed in HS300 for 1 day: aggregated particles (left), core-shell structure upon exposure to HS300 (right); **(C)** nZVI exposed in 1 mM sulfide ($S/Fe = 0.112$) and HS300 for 1

day: co-presence of residual nZVI and FeS (left), EDX of residual nZVI (right top), and EDX of FeS (right bottom).

Table S2. Surface element atomic percentage of pristine nZVI and nZVI exposed to incremental sulfide concentrations in HS300 for 1 day by XPS wide survey scan.

S/Fe ratio	Atomic ratio %									
	Fe2p	O1s	S2p	B1s	C1s	Ca2p	P2p	Si2p	Cu2p3	MgKLL
0 (Pristine nZVI)	27.8	27.4	N/D	19.2	25.6	N/D	N/D	N/D	N/D	N/D
0 (nZVI + HS300)	13.8	45.7	0.4	N/D	25.3	4.4	6.8	1.7	N/D	0.8
0.011 (nZVI + HS300 + 0.1 mM S ²⁻)	15.1	42.0	0.8	N/D	29.7	4.0	6.4	1.1	N/D	0.8
0.112 (nZVI + HS300 + 1 mM S ²⁻)	42.9	37.7	10.5	N/D	N/D	3.5	3.4	N/D	1.0	1.0
0.224 (nZVI + HS300 + 2 mM S ²⁻)	51.5	26.6	10.9	N/D	N/D	3.8	2.4	N/D	1.1	1.9
1.12 (nZVI + HS300 + 10 mM S ²⁻)	53.9	25.2	12.9	N/D	N/D	2.7	2.2	N/D	1.4	1.6

N/D: Not detectable above the signal background.

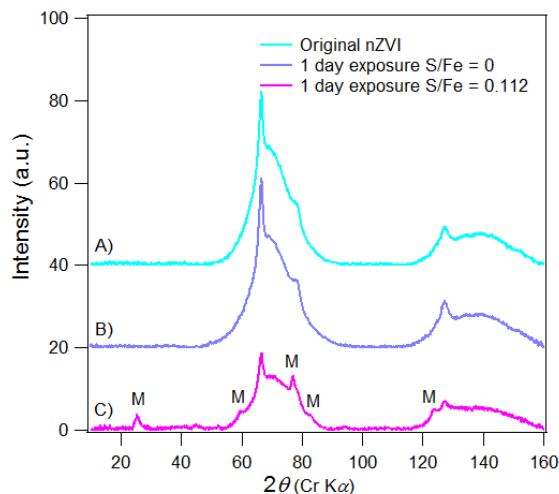


Figure S2. Micro-XRD pattern of (A) pristine nZVI, (B) nZVI in HS300 for 1 day (S/Fe = 0) and (C) nZVI exposed to 1 mM sulfide in HS300 for 1 day (M stands for mackinawite).

Table S3. Summary of μ XRD and Mössbauer data of pristine nZVI with comparisons to previously reported studies.

Sources	This study	Prior studies ^b of related nZVI (Fe ^{BH a})	Prior studies ^c of Fe-boron alloys
(μ)XRD	Less than 10% of the phase matches face cubic center (FCC) γ -iron best (represented by sharp peak in Figure S2). Broad humps represent poorly crystalline phase, which as smaller cell parameter than the sharp peak.	Predominantly body cubic center (BCC)- α iron	Amorphous
Mössbauer	Most consistent with amorphous iron ³	BCC- α iron	Amorphous

^a Fe^{BH} represents nZVI synthesized by borohydride reduction, adapted from Nurmi et al.⁴; ^b 5-7; ^c 8-10.

Discussion

Figure S1B shows that the nZVI exposed to HS300 media for 1 day retains the chainlike morphology similar to pristine nZVI (**Figure S1A**). The core-shell structure of individual

particle is also preserved. However, the thickness of the shell is much less uniform and generally thicker compared to the pristine nZVI, evidently due to more extensive growth of the FeO passive layer. This interpretation is supported by XPS survey scan that shows the increasing oxygen amount in sample exposed to HS300 only (**Table S2**). XPS survey scans also showed no boron in samples that were exposed to aqueous media, which can be attributed to the hydrolysis of Fe boride.⁹

Table S3 summarizes differences in the μ XRD and Mössbauer results between the present study and prior work. The μ XRD pattern of the pristine nZVI contained sharp peaks that were most consistent with an FCC lattice (**Figure S2A**). By contrast, most of the prior XRD characterizations of nZVI synthesized by NaBH_4 reduction suggest BCC α -iron.^{5,7} In this study, it was estimated that the sharp peaks that match FCC lattice best (**Figure S2A**) account for less than 10% of the total signal. The majority of the signal represented by the broad peaks cannot be identified with certainty, and could be amorphous or poorly crystalline material. Previous studies on Fe^{BH} also suggest that the XRD peak of Fe^{BH} is broader compared to typical α -iron, representing a distribution of crystallite size.^{4,5} Although the FCC lattice is typically found in γ -iron that is formed at high pressure and temperatures, FCC-modified iron may also arise as a result of alloying elements, most commonly carbon, at ambient conditions, especially when the particle size is small.¹¹ For the present nZVI samples, we speculate that boron incorporated into the nZVI shell has stabilized the FCC Fe lattice. The Mössbauer spectrum of the pristine nZVI exhibits broad features that are most consistent with amorphous Fe metal,³ which are clearly distinct from previously published Mössbauer spectra of nZVI made by borohydride reduction.^{6,7} However, in these two previous studies, the samples were prepared either by heat- or freeze-drying, which could easily be responsible for changing the crystallinity of the material.¹² In fact, several earlier studies using borohydride reduction to synthesize ultrafine particles of Fe-metal (metalloid) alloys with recovery by filtration have reported broad Mössbauer features similar to this study, and they also interpreted their results as indication that the freshly prepared material was amorphous.^{8,10} After annealing at high temperature, however, the spectra obtained in these studies^{8,10} showed features indicating transformation to more crystalline α -iron. Given that the flash drying protocol used in this study is essentially an anaerobic filtration,¹² the amorphous nature of the pristine nZVI observed here is reasonable.

In addition to post synthesis treatment, other experimental differences during the synthesis between our methods and those of previous studies could contribute to differences in the final product. One distinctive aspect of our method is the strong homogenization used during the introduction of NaBH_4 to FeCl_3 aqueous solution. This was done to mix the reagents rapidly and minimize aggregation of newly formed particles without the complications created by using a magnetic stir bar with magnetic nanoparticles. A variety of subjective, preliminary tests indicated that mixing with a homogenizer produced more reproducible dispersions of nZVI, but the specific effects of this on the particle composition and structure were not studied further.

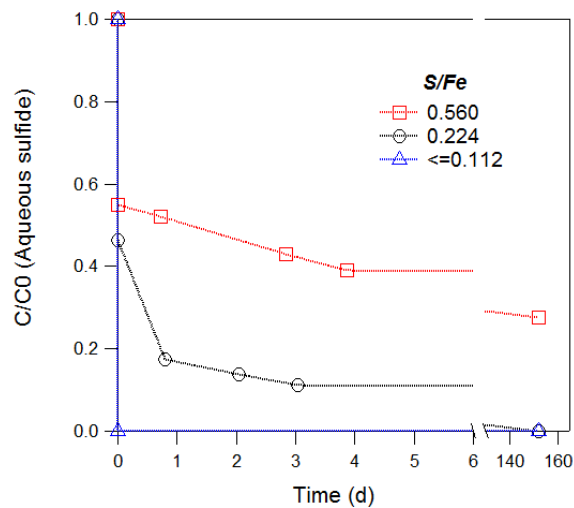


Figure S3. The kinetics of sulfide uptake by nZVI at various S/Fe ratios in HS300 (nZVI concentration: 0.2 g L^{-1} , sulfide dose: 0, 0.04, 0.08, 0.16, 0.2, 0.4, 0.8, and 2 mM, pH = 7.9, temperature = $27 \pm 0.5 \text{ }^\circ\text{C}$, aqueous sulfide concentrations in batches with sulfide dose below 0.8 mM were all below detection).

Control experiments without nZVI showed negligible changes of aqueous sulfide concentration over the sampling course (data not shown). At low S/Fe (≤ 0.112), aqueous sulfide was removed to below the detection limit within 5 min after sulfide addition (**Figure S3**).

However, at relatively high S/Fe (0.224 and 0.56), the kinetics of sulfide removal from solution exhibited two phases, with about half of the input sulfide removed rapidly followed by a gradual decrease over a much longer period (**Figure S3**). The initial, fast stage likely corresponds to instantaneous sulfide adsorption onto the surface Fe oxides coating on nZVI, forming a surface

complex of Fe(II)–HS⁻.¹³ A similar process has been postulated to be the initial step in mackinawite formation on iron oxides in natural sulfidic environments.^{14, 15} The later stage of sulfide removal reflects relatively slow formation of FeS precipitates. At S/Fe = 0.56, significant residual aqueous sulfide was detected even after 150 days of exposure, indicating incomplete transformation of nZVI to FeS.

2. Batch Tc Reduction Kinetics under High Fe dose (0.5 g/L)

Results

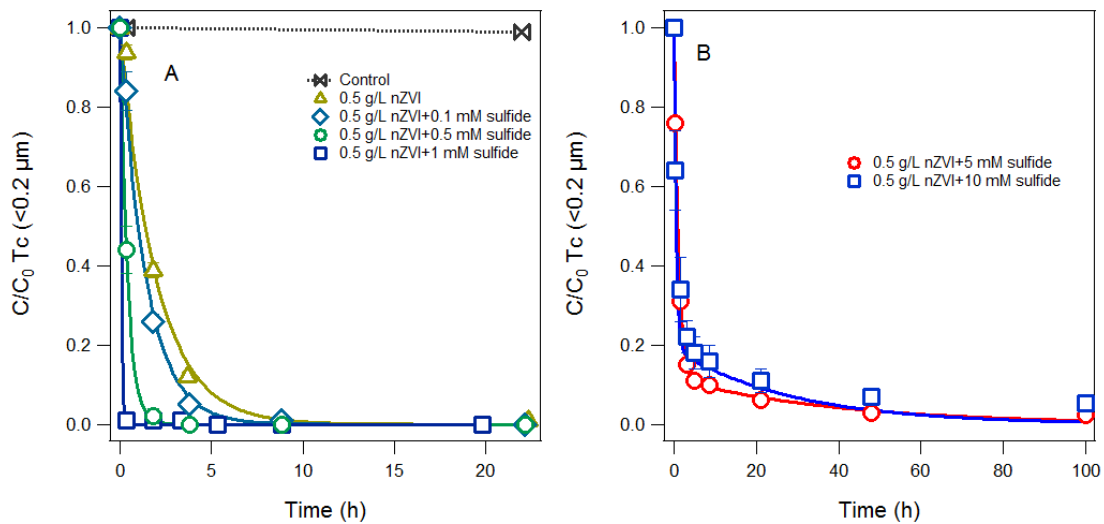


Figure S4. Tc sequestration kinetics at high nZVI dose (0.5 g L^{-1}): **(A)** low S concentration (0.1 mM to 1 mM) and **(B)** high sulfide concentration (5 and 10 mM) (S/Fe ratio has the same range as **Figure 2**. Error bars represent the standard error from duplicates).

In these high nZVI dose experiments, the batch reactors were kept still without external mixing. Therefore, the reaction rate was significantly slower than the reaction rate presented in **Figure 4**, even though the nZVI and sulfide doses were higher. However, it is important to note that the general observation of these experiments is consistent with what was shown in **Figure 4**: at low S/Fe ratios, the reaction rate increased as S/Fe increased but higher S/Fe resulted in inhibition of Tc removal. The higher residual Tc concentration (< 0.2 μm) observed at 5 and 10 mM sulfide concentrations were probably due to higher residual sulfide concentration.

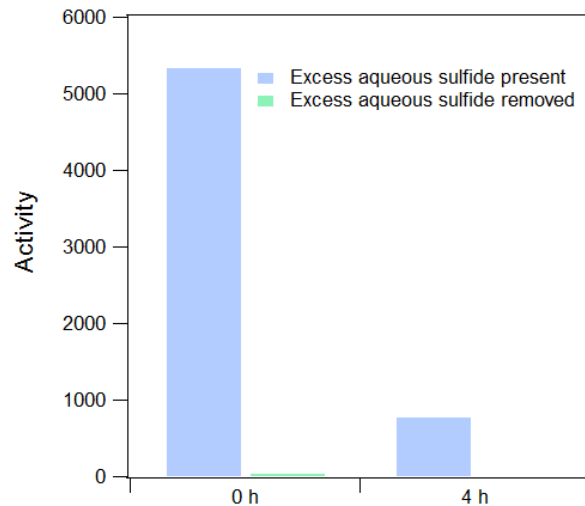


Figure S5. Tc remaining in solution in the presence and absence of excess aqueous sulfide (Tc concentration is represented by counts per minute from liquid scintillation; Two batch reactors were prepared by exposing 0.5 g L^{-1} nZVI to 10 mM sulfide in HS300 for 1 day at pH = 7.9; Before Tc addition, excess of aqueous sulfide was removed in one of the bottles by filtration and the recovered solid was resuspended in HS300).

Figure S5 shows the preliminary results where Tc removal rate was compared in the presence and absence of excess aqueous sulfide. Tc ($< 0.2 \text{ }\mu\text{m}$) was quantified by using direct reading of the radioactivity (CPM). It clearly shows that when excess of aqueous sulfide was removed, Tc removal (blue bars) was much faster compared to the batch where excess of aqueous sulfide was present (green bars), and the removal rate is comparable to the lower S/Fe ratio cases (**Figure 4** and **Figure S4A**). This suggests that the inhibition of Tc removal resulted from excess aqueous sulfide.

3. Evidence of Colloidal Tc Formation

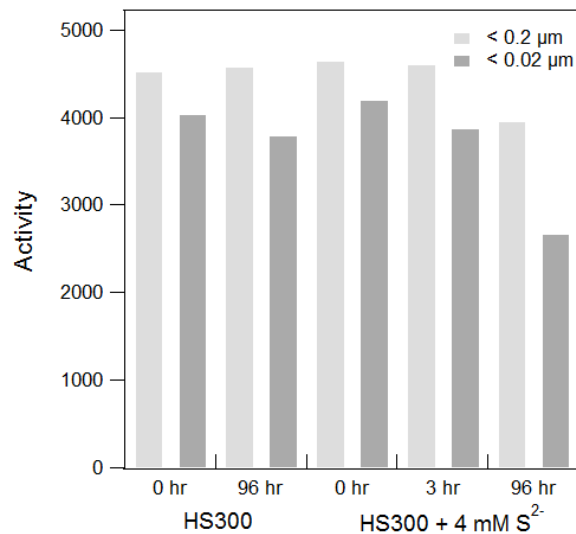


Figure S6. Tc concentration in the presence and absence of sulfide (activity in 0.2 and 0.02 μm filtrate was compared to differentiate colloidal Tc from dissolved TcO₄⁻).

4. SEMs and TEMs of Sulfidated nZVI Exposed to TcO₄⁻

Method

Scanning Electron Microscopy (SEM).

For Tc-containing material, a 5 μL drop was placed onto a silicon wafer and then anaerobically dried in the glove bag for scanning electron microscopy. The samples were coated using the Poloran carbon coater, and ~5–10 nm carbon coating was applied to each sample. Samples were analyzed in a FEI Quanta 3DFEG scanning electron microscope equipped with an Oxford 80 mm² SDD detector and INCA software. Initially 20 keV was used to analyze the samples but later changed to 30 keV to pick up the Tc L 18.2 line to confirm Tc was present since the M line overlaps with sulfur which is between 2.3–2.5 keV. Surface tomography of the samples was obtained at 5 keV since 20–30 keV destroys any surface tomography of the material.

Transmission Electron Microscopy (TEM).

For Tc-containing material, the sample preparation involved applying a 5 μL drop of material aqueous suspension to a 200-mesh copper TEM grid with carbon-coated formvar support film, (Electron Microscopy Sciences, Hatfield, PA). After 1 min, the excess liquid was removed by wicking, and the sample on a grid was anaerobically dried in the glove bag atmosphere (Coy Laboratories, Grass Lake, MI). The sample was anaerobically transferred to the TEM laboratory. Final loading of the sample on the holder required short period exposure to aerobic conditions. The prepared samples were imaged with JEOL 2010F transmission electron microscope operating at 200kV, coupled with INCA energy-dispersive spectroscopy (EDS) system (Oxford Instruments, UK) for elemental analysis.

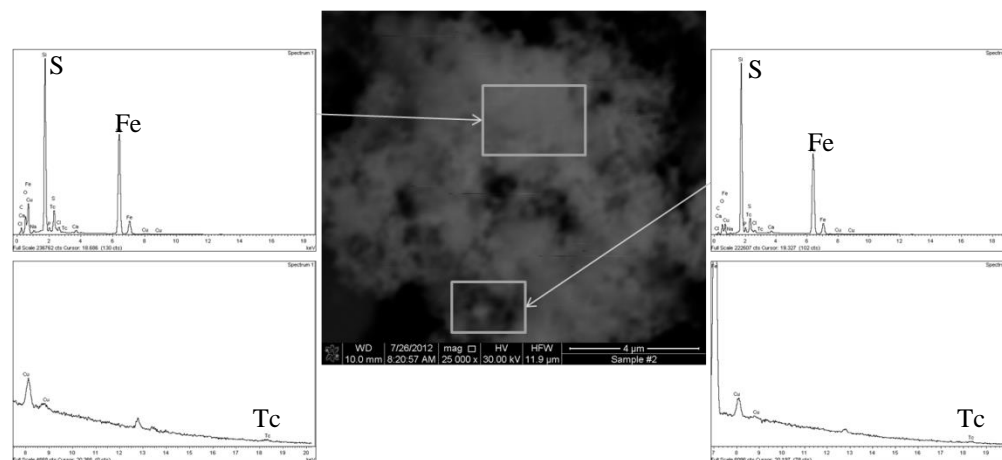


Figure S7. A Back scattered scanning electron micrograph (middle) of sulfidated nZVI ($S/Fe = 0.112$) exposed to $50 \mu\text{M TcO}_4^-$ and corresponding energy dispersive x-ray spectra (EDX) (top left: spectra 1; bottom left: enlarged spectra 1; top right: spectra 2; bottom right: enlarged spectra 2).

The chemical heterogeneity shown at the scale of SEM was not as significant as that seen by TEM (**Figure 5**). S/Fe ratios measured at multiple areas by EDX (**Figure S7** and other spectra (data not shown)) were around the input S/Fe ratio, which equals to 0.112. As a result, SEM did not show a significantly different Tc distribution pattern.

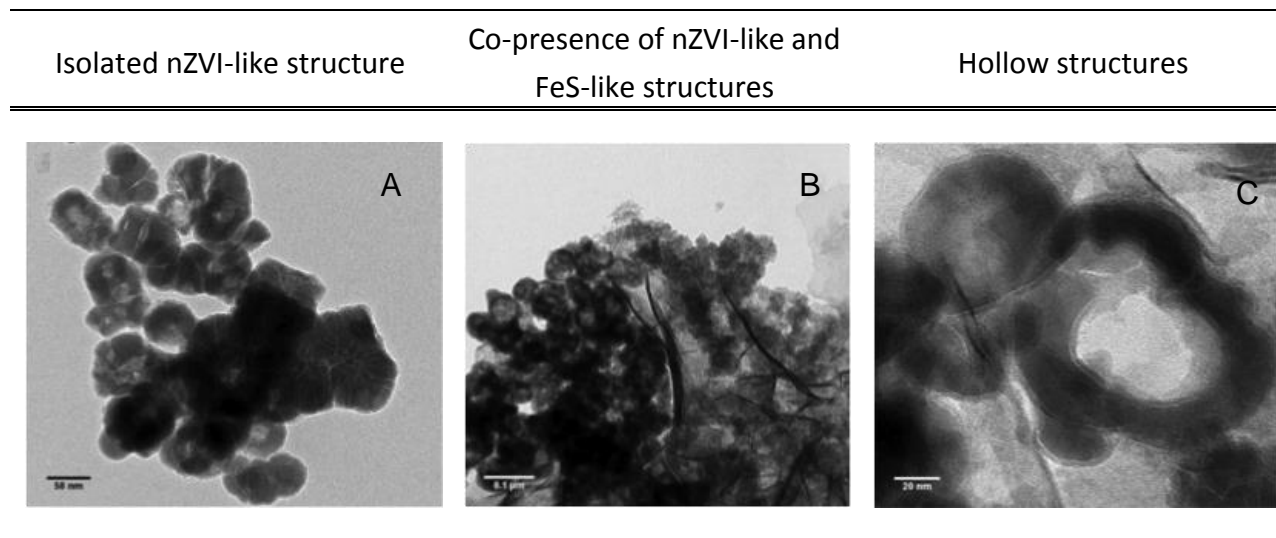


Figure S8. Transmission electron micrographs of representative morphologies of sulfidated nZVI exposed to TcO_4^- (images were collected on the same sample in **Figure 5**: $[\text{TcO}_4^-] = 50 \mu\text{M}$, $[\text{nZVI}] = 0.2 \text{ g L}^{-1}$, $[\text{S}^{2-}] = 0.4 \text{ mM}$, $\text{S/Fe} = 0.112$, $\text{pH} = 7.9$).

5. Additional XAS information

Method

Tc XAS samples were prepared by reacting $8.4 \mu\text{M}$ TcO_4^- with 0.5 g L^{-1} nZVI pre-exposed to 0–10 mM sulfide. After greater than 99% Tc ($< 0.2 \mu\text{m}$) removal, Tc-containing solids were centrifuged and loaded as a concentrated slurry/paste into single slot Teflon holders. The holders were then sealed with a single layer of Kapton tape and further contained inside a heat-sealed polypropylene bag. Samples were kept in an anaerobic chamber prior to the measurements and under a continuous He purge while collecting the XAS spectra. XAS measurements were taken at the Tc K-edge and were collected at the Stanford Synchrotron Radiation Lightsource (SSRL) on beamline 4-1 and 11-2. Spectra were measured at room temperature in fluorescence mode using a 13 (30) element solid state detector (Ge), and a N_2 -cooled Si (220) double crystal monochromator, detuned for 20% for harmonic rejection. Energy calibration was internally measured during each scan using a Mo metal foil (Mo K-edge energy 20 KeV).

Linear combination fitting of EXAFS was performed in ATHENA for samples with S/Fe ratios ranging from 0.0056 to 0.56 using samples with S/Fe = 0 and 1.12 as two end members, respectively. The values of each component were normalized to the total spectral weight sum

from the components used in the linear combination. The total spectral weight sum ranged from 0.85 to 1 (without any constraining of the sum).

Additional results

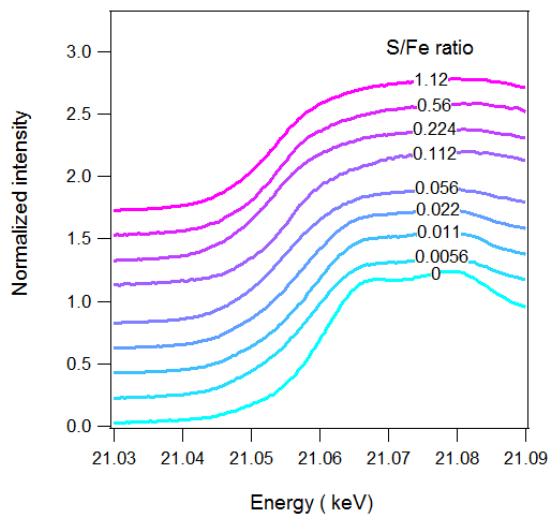


Figure S9. Tc K-edge XANES of Tc immobilized at incremental S/Fe ratios (The spectra were collected on the same set of samples as in **Figure 7**).

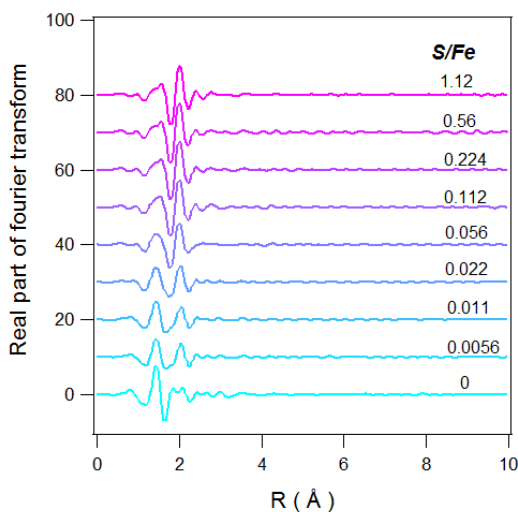


Figure S10. Real part of Fourier transform of EXAFS of Tc reduced at incremental S/Fe ratios (The spectra were collected on the same set of samples in **Figure 7**).

Table S4. Tc-EXAFS shell by shell fit for Tc reduced at S/Fe = 0 and 1.12 (*N*: coordination number; *D*: interatomic distance; σ^2 : Debye-Waller factor; Standard deviation is in parenthesis)

nZVI + Tc + 0 mM S ²⁻			nZVI + Tc + 10 mM S ²⁻		
	<i>N</i>	†6		<i>N</i>	‡2
<i>Tc-O1</i>	<i>D</i> (Å)	2.02(1)	<i>Tc-S1</i>	<i>D</i> (Å)	2.30(2)
	σ^2 (Å ²)	0.006(1)		σ^2 (Å ²)	0.003(2)
<i>Tc-Tc1</i>		†1	<i>Tc-S2</i>		‡4
		2.44(3) 0.011(1)			2.47(1) 0.003(2) ^A
<i>Tc-Tc2</i>		†1	<i>Tc-Tc1</i>		‡2
		3.19(4) 0.011(3) ^a			2.39(1) 0.005(2) [†]
<i>Tc-O2</i>		†4	<i>Tc-Tc2</i>		†1
		3.17(4) 0.009(2)			2.58(2) 0.005(2) ^B
<i>Tc-O3</i>		†4	<i>Tc-S3</i>		‡2
		3.56(8) 0.009(2) ^b			3.13(1) 0.005(2) ^C
<i>Tc-Tc3</i>		†4	<i>Tc-S4</i>		†1
		3.71(2) 0.025(6)			3.78(1) 0.005(2) ^C
<i>Tc-O1-O1-Tc</i>		6 ^d	<i>Tc-S5</i>		†1
		4.06(2) ^d 0.011(2) ^d			3.98(3) 0.005(2) ^C
<i>Tc-Tc4</i>		†4	<i>Tc-Tc3</i>		‡2
		4.01(2) 0.025(6) ^c			3.63(1) 0.007(2) ^D
			<i>Tc-Tc4</i>		†1
					3.81(2) 0.007(2) ^D

† Coordination numbers maintained to crystallographic value of TcO₂.

‡ Coordination numbers maintained to crystallographic value of TcS₂

^a $\sigma_{Tc-Tc1} = \sigma_{Tc-Tc2}$, ^b $\sigma_{Tc-O3} = \sigma_{Tc-O3}$, ^c $\sigma_{Tc-Tc4} = \sigma_{Tc-Tc3}$,

^d Multiple scattering N, σ , and d constrained to Tc-O1 shell distances.

^A $\sigma_{Tc-S1} = \sigma_{Tc-S2}$, ^B $\sigma_{Tc-Tc1} = \sigma_{Tc-Tc2}$, ^C $\sigma_{Tc-S} = \sigma_{Tc-Tc1+0.002}$, ^D $\sigma_{Tc-Tc} = \sigma_{Tc-Tc1+0.002}$

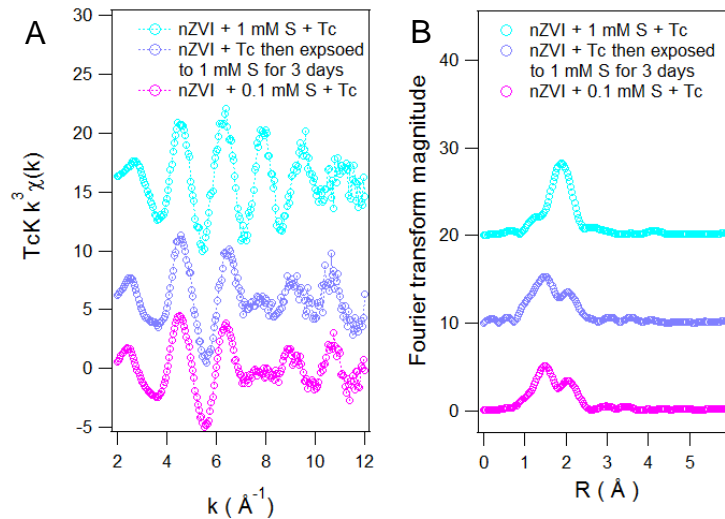


Figure S11. (A) Tc K-edge EXAFS and (B) the respective Fourier transform of Tc reduced by nZVI first then exposed to 1 mM sulfide for 3 days (spectra for Tc reduced under S/Fe = 0.011 and 0.112 were used for comparison).

6. Geochemical Speciation Modeling of Tc/Fe/S system

Methods

Geochemical speciation modeling was performed using the ACT subset of the Geochemist's Workbench modeling package, release 8.0 (RockWare Inc., Golden, CO) with the thermodynamic constants given in the thermo.com.v8.r6+ dataset. Additional data for FeS was adapted from Davison et al.¹⁶ and input into the dataset. Speciation diagrams for Fe/Tc/S in artificial Hanford groundwater system (HS300) were generated using the concentrations listed in **Table S1**. In the generation and interpretation of these diagrams, it was assumed that activity (α) was equal to concentration.

Results

The Fe/Tc speciation diagram was constructed in a way that is similar to the experimental design. $[\text{HS}^-]$ instead of $[\text{H}^+]$ was used as x-axis variable in order to represent the evolution of sulfidogenic conditions. Equilibrium approach was used to calculate Fe and Tc speciation and elucidate possible Tc sequestration pathways in the presence of nZVI and sulfide. The diagram suggested that the hypothetical Tc sequestration pathways presented in **Figure 1** are thermodynamically possible. $\text{TcO}_2 \cdot n\text{H}_2\text{O}$ is the predominant reduced Tc phase when $\log a[\text{HS}^-]$

is less than -23. Beyond that value, TcS_2 becomes the dominant reduced Tc phases. The boundary line between Tc_2S_7 and TcS_2 has a negative slope with respect to $\log a[\text{HS}^-]$. As sulfide concentration further increases to the range of this study (shaded area), both TcS_2 and Tc_2S_7 are the dominant Tc phases, and this area coincidentally overlaps with the stability region of FeS. The diagram also indicates the possibility of transformation from $\text{TcO}_2 \cdot n\text{H}_2\text{O}$ to TcS_2 or from Tc_2S_7 to TcS_2 . The first pathway is especially important in real remedial practice because $\text{TcO}_2 \cdot n\text{H}_2\text{O}$ is expected to be the dominant Tc reduced phase before sulfate reduction develops. This pathway has also been confirmed by XAS results (See **Figure S11**).

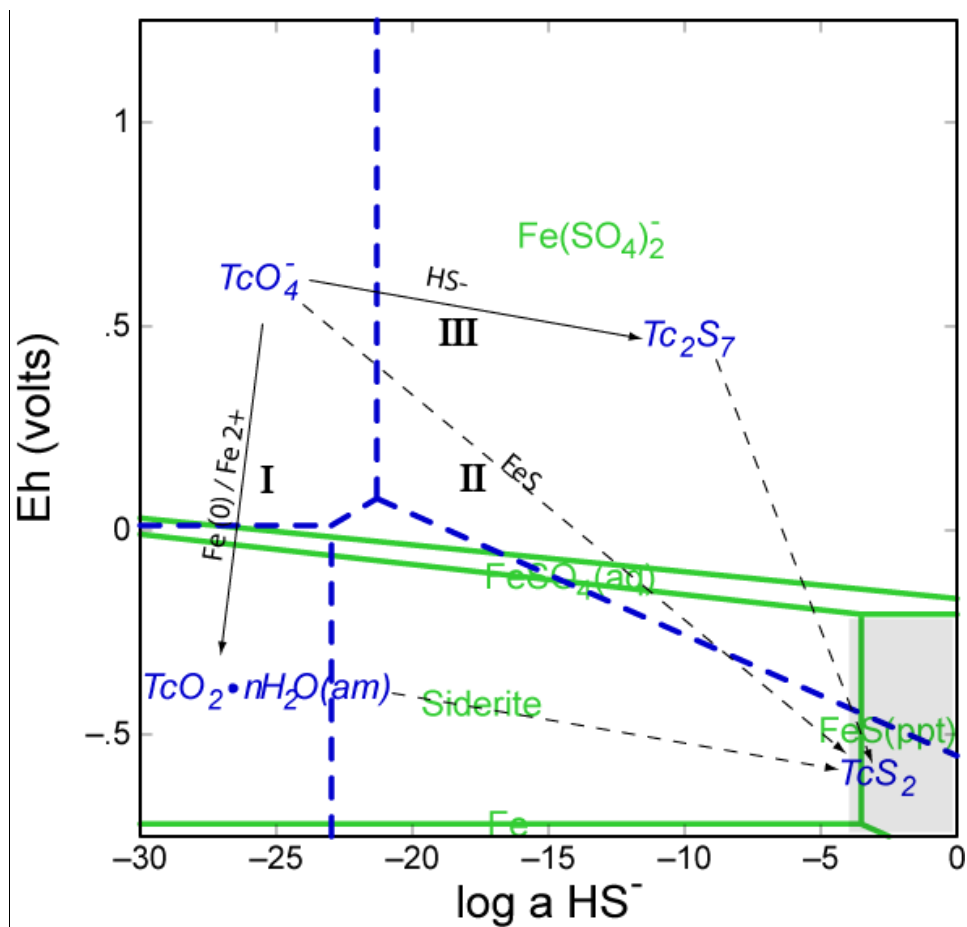


Figure S12. Eh vs. $\log a(\text{HS}^-)$ of Fe/S/Tc speciation diagram in HS300 (Fe and Tc speciation diagrams were independently constructed and overlaid with each other: areas with green boundaries are the Fe stability regions and areas with blue boundaries are the Tc stability regions; shaded area represents the experimental conditions in terms of sulfide concentration and expected Eh range; Solid arrows represent the known reaction pathways whereas dashed arrows represents hypothetical reaction pathways; Process I, II, and III correspond to the reaction pathways in **Figure 1**; Model input: $[\text{TcO}_4^-] = 10 \mu\text{M}$, $\text{pH} = 7.9$, $T = 25 \text{ }^\circ\text{C}$).

References in supporting information

- (1) Lee, J.-H.; Fredrickson, J. K.; Kukkadapu, R. K.; Boyanov, M. I.; Kemner, K. M.; Lin, X.; Kennedy, D. W.; Bjornstad, B. N.; Konopka, A. E.; Moore, D. A.; Resch, C. T.; Phillips, J. L. Microbial reductive transformation of phyllosilicate Fe(III) and U(VI) in fluvial subsurface sediments. *Environ. Sci. Technol.* **2012**, *46*, 3721-3730.
- (2) Peretyazhko, T. S.; Zachara, J. M.; Kukkadapu, R. K.; Heald, S. M.; Kutnyakov, I. V.; Resch, C. T.; Arey, B. W.; Wang, C. M.; Kovarik, L.; Phillips, J. L.; Moore, D. A. Pertechetate (TcO_4^-) reduction by reactive ferrous iron forms in naturally anoxic, redox transition zone sediments from the Hanford Site, USA. *Geochim. Cosmochim. Acta* **2012**, *92*, 48-66.
- (3) Long, G. J.; Hautot, D.; Pankhurst, Q. A.; Vandormael, D.; Grandjean, F.; Gaspard, J. P.; Briois, V.; Hyeon, T.; Suslick, K. S. Mössbauer-effect and x-ray absorption spectral study of sonochemically prepared amorphous iron. *Phys. Rev. B* **1998**, *57*, 10716-10716.
- (4) Nurmi, J. T.; Tratnyek, P. G.; Sarathy, V.; Baer, D. R.; Amonette, J. E.; Pecher, K.; Wang, C.; Linehan, J. C.; Matson, D. W.; Penn, R. L.; Driessen, M. D. Characterization and properties of metallic iron nanoparticles: spectroscopy, electrochemistry, and kinetics. *Environ. Sci. Technol.* **2005**, *39*, 1221-1230.
- (5) Wang, Q.; Snyder, S.; Kim, J.; Choi, H. Aqueous ethanol modified nanoscale zerovalent iron in bromate reduction: synthesis, characterization, and reactivity. *Environ. Sci. Technol.* **2009**, *43*, 3292-3299.
- (6) Kanel, S. R.; Grenèche, J.-M.; Choi, H. Arsenic(V) removal from groundwater using nano scale zero-valent iron as a colloidal reactive barrier material. *Environ. Sci. Technol.* **2006**, *40*, 2045-2050.
- (7) Glavee, G. N.; Klabunde, K. J.; Sorensen, C. M.; Hadjipanayis, G. C. Chemistry of borohydride reduction of iron(II) and iron(III) ions in aqueous and nonaqueous media - formation of nanoscale Fe, FeB, and Fe₂B powders. *Inorg. Chem.* **1995**, *34*, 28-35.
- (8) Forster, G. D.; Fernández Barquín, L.; Bilsborrow, R. L.; Pankhurst, Q. A.; Parkin, I. P.; Steer, W. A. Sodium borohydride reduction of aqueous iron-zirconium solutions: chemical routes to amorphous and nanocrystalline Fe-Zr-B alloys. *J. Mater. Chem.* **1999**, *9*, 2537-2544.
- (9) Corrias, A.; Ennas, G.; Musinu, A.; Marongiu, G.; Paschina, G. Amorphous transition metal-boron ultrafine particles prepared by chemical methods. *Chem. Mater.* **1993**, *5*, 1722-1726.

- (10) Van Wonterghem, J.; MØrup, S.; Koch, C. J. W.; Charles, S. W.; Wells, S. Formation of ultra-fine amorphous alloy particles by reduction in aqueous solution. *Nature* **1986**, *322*, 622-623.
- (11) Wei, B.; Shima, M.; Pati, R.; Nayak, S. K.; Singh, D. J.; Ma, R.; Li, Y.; Bando, Y.; Nasu, S.; Ajayan, P. M. Room-temperature ferromagnetism in doped face-centered cubic Fe nanoparticles. *Small* **2006**, *2*, 804-809.
- (12) Nurmi, J.; Sarathy, V.; Tratnyek, P.; Baer, D.; Amonette, J.; Karkamkar, A. Recovery of iron/iron oxide nanoparticles from solution: comparison of methods and their effects. *J. Nanopart. Res.* **2011**, *13*, 1937-1952.
- (13) Hansson, E. B.; Odziemkowski, M. S.; Gillham, R. W. Formation of poorly crystalline iron monosulfides: surface redox reactions on high purity iron, spectroelectrochemical studies. *Corros. Sci.* **2006**, *48*, 3767-3783.
- (14) Rickard, D.; Luther III, G. W. Chemistry of iron sulfides. *Chem. Rev.* **2007**, *107*, 514-562.
- (15) Morse, J. W.; Millero, F. J.; Cornwell, J. C.; Rickard, D. The chemistry of the hydrogen sulfide and iron sulfide systems in natural waters. *Earth-Sci. Rev.* **1987**, *24*, 1-42.
- (16) Davison, W.; Phillips, N.; Tabner, B. J. Soluble iron sulfide species in natural waters: reappraisal of their stoichiometry and stability constants. *Aquat. Sci.* **1999**, *61*,